Optical Properties of Au Nanoparticles Included in Mesoporous TiO₂ Thin Films: A Dual Experimental and Modeling Study

V. M. Sánchez,[†,‡] E. D. Martínez,[†] M. L. Martínez Ricci,[§] H. Troiani,[∥] and G. J. A. A. Soler-Illia*[,†,‡]

[†]Gerencia Química, Comisión Nacional de Energía Atómica, Centro Atómico Constituyentes, Av. Gral. Paz 1499 (B1650KNA), San Martín, Buenos Aires, Argentina

[‡]Departamento de Química Inorgánica, Analítica y Química Física, Facultad de Ciencias Exactas y Naturales, Universidad de Buenos Aires, Ciudad Universitaria, Pabellón 2, C1428EHA, Buenos Aires, Argentina

[§]INQUIMAE, CONICET, Ciudad Universitaria, Pabellón 2, C1428EHA, Buenos Aires, Argentina

[∥]Comisión Nacional de Energía Atómica, Centro Atómico Bariloche, and Instituto Balseiro, San Carlos de Bariloche, 8400, Argentina

Ⓢ *Supporting Information*

ABSTRACT: Gold nanoparticles (NP) were synthesized inside ordered mesoporous TiO₂ thin films (MTTF) by stepwise reduction of AuCl₄⁻ with NaBH₄. This leads to an optical material (Au@TiO₂) of interest for plasmonic applications. The films (pure titania or gold-titania nanocomposites) were thoroughly characterized by UV–visible and ellipsometry spectroscopies. The dielectric function of the MTTF, considered as the dielectric environment in which the NP are embedded, was acquired by ellipsometry and rationalized by the asymmetric Bruggeman model as an

effective medium formed by the mixture of dense TiO₂ and air. Nanocomposite Au@TiO₂ systems present an isotropic dispersion of Au NP in the 5−8 nm range. The UV–visible spectra obtained with a low nanoparticle filling fraction of the pore volume ($f_{NP} < 2\%$) are accurately reproduced by both Maxwell−Garnett (MG) and Mie theories. Accurate and coincident values of f_{NP} and NP size are obtained by this method. The dielectric function of Au NP used in this work was studied in detail; in particular, the interface damping parameter related to the NP/MTTF interface was determined by comparison with TEM microscopy. The potential of the ellipsometry technique to determine the material plasmonic response, and its correspondence with the UV–visible spectra, are discussed. This spectroscopy technique opens the possibility to study the plasmon response of the material to changes in the environment due to the presence of vapors, and other in situ experiments, as well as to provide nanostructural information of metallic nanoparticles (NP size, interparticle distance, number of NP) with well-defined spatial localization in a multilayered system.
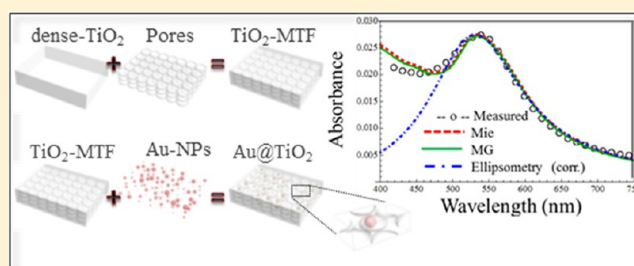
1. INTRODUCTION

Mesoporous thin films are established as a growing field in nanochemistry due to the high level of control attainable in the pore size, the organization of the porous framework on the mesoscopic scale, and the possibility of controlling its accessibility. Those aspects are of paramount importance in the design of advanced catalysts, sensors, selective membranes and other devices exploiting related surface chemistry phenomena. The special case of TiO₂ nanostructures and surfaces has been reviewed several times[1,2] and recently it has been the exclusive subject of a special issue,[3] showing the relevance of this material in photochemistry applications like photovoltaics[4] and photocatalysis.[5]

Independently, noble metal nanoparticles, mainly made of silver and gold, possess unique optical properties arising from the excitation of Localized Surface Plasmon Resonance (LSPR) that takes place at optical frequencies. Several applications regarding the dependence of the plasmon frequency with its dielectric environment are of interest in technological develop-

ments of optical-based sensors[6−10] and Surface Enhanced Raman Scattering (SERS) substrates.[11−15] The ability to locate NP in a solid matrix, avoiding their aggregation without affecting the accessibility of the analytes of interest, is fully satisfied by the use of a mesoporous framework as a host material for their inclusion with NP, which can be done either by infiltrating the mesostructure with preformed NP,[16] by controlling their nucleation and growth from the adsorption of soluble precursors,[17] by electrodeposition,[18] or by photocatalytic-assisted deposition.[19] Recently, gold NP of controlled shapes covered by a mesoporous film were produced,[20] and the possibility of in situ monitoring of solvent evaporation in a sensitive way was demonstrated.[21] In particular, Au@TiO₂ nanocomposites have been proven to account for light driven charge transfer processes both from the NPs to the oxide and

vice versa. The first mechanism can enhance the photocatalytic performance by accumulating and discharging electrons under on−off cycles of UV light exposure;[22] in the second case, plasmon excitation induces electron transfer from the NPs to the TiO$_2$, resulting in a visible light driven photoanode able to oxidize H$_2$O in a water splitting reaction.[23] Solar cells involving plasmonic components have also been pursued.[24,25] A SERS effect has also been proven to take place in thin films nanostructures composed of Au NP and TiO$_2$ nanotubes.[26] In addition, Au nanoparticles embedded into MTTF have proven to be highly active for the water gas shift reaction in an idealized reaction gas mixture, presenting a remarkable stability.[27] The photocatalytic performance of MTTF loaded with Au NP have also been reported for the oxidation of phenol and the reduction of chromium cations.[28]

In all of these cases, the characterization and interpretation of the optical properties is an essential issue for the tailored design of this nanocomposite material. Optical properties give a sound information about the size and the nanoparticle loading of a film, which is an essential issue for Surface Plasmon Resonance (SPR), SERS, or catalytic applications. UV−visible spectrophotometry[29,30] and spectroscopic ellipsometry[31,32] have been extensively used as a basic characterization tool of NP embedded within sol−gel derived thin films.[33,34] In the case of mesoporous thin films, the plasmon band position and intensity are usually interpreted as a consequence of the actual particle sizes and mesoporous matrix refractive index, with no further analysis.[18,35] Therefore, there is a need for the development of simple theories that permit to extract structural information of the NP and the mesoporous matrix properties from the nanocomposite spectra. In addition, this theory should be able to reconcile and exploit the information obtained by UV−vis spectroscopy and ellipsometry. These aspects have not been extensively treated, to the best of our knowledge, in the current literature.

The aim of this work is to formulate a formal description of the origin and interpretation of the data obtained by each technique and to propose a mechanism by which this dual characterization can provide valuable information about the particle size and the volume filling fraction of the metal phase in the composite material. For this purpose, a reference system based on Pluronics F127 templated TiO$_2$ mesoporous thin films loaded with gold NP will be described as a collection of particles in a dielectric environment for which Mie theory[36] can be applied, and also by an effective medium theory, namely Maxwell−Garnett,[37] whose calculation provides an effective dielectric function that can be directly measure by ellipsometry. It is important to remark that the effective medium that surrounds metallic NP is experimentally determined through ellipsometry measurements and is not taken as a wavelength independent value, extracted from tabulated data, or inferred from the plasmon peak position, as it is usually reported.[38,39] This procedure permits a thorough yet simple modeling of the optical parameters of these nanocomposites.

2. EXPERIMENTAL SECTION

2.1. Synthesis. *2.1.1. TiO$_2$ Mesoporous Thin Films.* Mesoporous TiO$_2$ thin films were produced by combining a sol−gel chemistry route with self-assembly of surfactant templates, in the strategy known as Evaporation Induced Self Assembly (EISA).[40,41] In a typical synthesis, Pluronics F127 (Sigma, PEO$_{106}$PPO$_{70}$PEO$_{106}$) was added to an ethanol solution of titanium tetrachloride (Merck, TiCl$_4$). Water was

subsequently added under strong agitation in order to dissolve the surfactant. The final molar ratio TiCl$_4$:EtOH:F127:H$_2$O were 1:40:0.005:10. Soda-lime glass slides were used as substrates for the deposition of the mesoporous films. The glass slides, previously washed with acetone, ethanol and water, and dried at 60 °C, were dipped into the sol heated up to 32 °C, and extracted at a constant withdrawal rate of 1 mm·s^{-1}. The relative humidity (RH) in the dip-coater chamber was set at 35%. After the dip-coating process was complete, the freshly deposited film was removed from the reverse side of the slides by gently rinsing with water and alcohol. Films were then placed in a closed chamber at 50% of controlled RH at room temperature for 24 h to promote the stabilization of the mesostructure. Stabilized films were then submitted to a thermal treatment of 30 min at 60 °C, and 30 min at 130 °C, triggering Ti−O−Ti condensation, and finally calcined at 350 °C for 2 h, for the removal of the polymeric surfactant and further consolidation of the solid structure.[42] The physical parameters of these films can be controlled with high accuracy and reproducibility and a narrow (approximately monodisperse) distribution of pore sizes can be achieved. Film thickness and porosity can be tuned by means of the withdrawal rate in the dip-coating process and the proper election of the templating agent respectively. Parameters like pore and neck size, accessible volume and thickness of the mesoporous films can be measured by ellipso-porosimetry (EP, see below).[43]

Dense titania films were synthesized by the same sol−gel procedure from a sol of the same composition but in the absence of the templating agent. After deposition through dip-coating at 1 mm·s^{-1} and submission to equal thermal treatment, the nonmesoporous TiO$_2$ films (TNM) result in thinner thickness compared to the mesoporous ones.

A bilayered mesoporous structure formed by a TiO$_2$ mesoporous film layer deposited over a preformed layer of mesoporous SiO$_2$ on a glass substrate, was synthesized as follows: a sol with molar ratio composition TEOS:EtOH:CTAB:HCl:H$_2$O 1:20:0.1:0.004:5, where TEOS (tetraethyl orthosilicate) is the Si precursor and CTAB (cetyltrimethylammonium bromide, C$_{16}$H$_{33}$N(CH$_3$)$_3$Br) acts as the templating agent, was dip-coated at 1 mm·s^{-1} and stabilized at 200 °C for 24 h. After this, the deposition of TiO$_2$ from the described sol was performed as mentioned before. This bilayer preparation procedure was reproduced from previous works of the group.[44]

2.1.2. Formation of Gold NP. The infiltration of MTTF with gold nanoparticles was achieved by an iterative two-step method that consists in the adsorption of a gold precursor on the mesopore surface, and its subsequent reduction with NaBH$_4$. The film was immersed during one minute in a 1 mM solution of HAuCl$_4$·3H$_2$O (Sigma-Aldrich) at pH 4 for the adsorption of Au(III) species on the positively charged surface of TiO$_2$. After that residence time, the film was removed and dried under air flow. The film was then immersed for another minute in a 1 mM NaBH$_4$ freshly prepared solution for the reduction of the adsorbed AuCl$_4^-$ ion, and finally rinsed with water. This procedure, referred to as a reduction step (RS), can be repeated as many times as desired increasing the filling fraction of the mesoporous framework (see Scheme 1). A pink color due to LSPR of gold nanoparticles arises after three steps of reduction.

2.2. Characterization. UV−vis spectrophotometry. Optical absorption of the mesoporous films deposited on glass substrates was followed by conventional UV−vis in an HP

Scheme 1. Synthesis of Au NP Embedded in the MTTF by Subsequent Reduction Steps
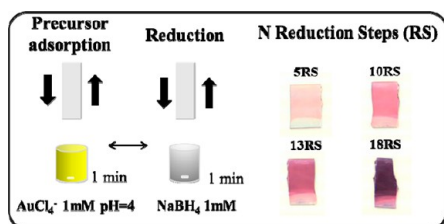
Agilent 8453 spectrophotometer in absorbance mode. The measurements were made by using as control or reference the same mesoporous film without the gold infiltration. Special attention was taken to provide a normal incidence of the light beam on the sample.

2.2.1. Spectrometric Ellipsometry and Ellipsoporosimetry. The mesoporous thin films without infiltration were first characterized by spectrometric ellipsometry (SE). This technique allows the determination of the thickness and optical constants, such as dielectric function and refractive index. In SE, the change in the polarization state of an impinging polarized light (with *s* and *p* components)—at off-normal incidence—over a film or surface is measured for a range of wavelengths. For isotropic materials, the ratio between reflection coefficients for each polarization mode, r_p and r_s, can be expressed as follows:[45]

$$\rho = \frac{r_p}{r_s} = \tan(\psi)e^{-i\Delta} \tag{1}$$

The quantities Δ and Ψ correspond to the phase difference and the amplitude ratio of the reflection coefficients, respectively. Since the change of these quantities depends on the dielectric constants of the materials involved, and film thickness for every wavelength, a model must be proposed to analyze the data and determine the complex dielectric function of the materials, $\varepsilon = \varepsilon_1 + i\varepsilon_2$. The refractive index ($n = n_r + i\kappa$) can be calculated by the following:

$$n_r = \sqrt{\frac{\varepsilon_1}{2} + \frac{1}{2}\sqrt{\varepsilon_1^2 + \varepsilon_2^2}} \; ; \; \kappa = \sqrt{\frac{-\varepsilon_1}{2} + \frac{1}{2}\sqrt{\varepsilon_1^2 + \varepsilon_2^2}} \tag{2}$$

The Cauchy[46] model was used to describe TiO$_2$ mesoporous thin films at wavelengths in which no absorption takes place. The LSPR due to the presence of the nanoparticles is described by a Lorentz oscillator as following the works of Oates[47] and Kürbitz et al.[33]

The pore volume and pore size of the obtained films were assessed by ellipsoporosimetry (EP). This technique consists of performing SE measurements in a chamber of controlled water vapor pressure. By the use of a Lorentz–Lorenz effective medium theory, a water adsorption isotherm is obtained from which the total accessible volume can be extracted; the pore size distribution can be obtained from the adsorption isotherm through the Kelvin equation. The measurements were performed in a commercial SOPRA GES5-A multispectral ellipsometer in the microspot configuration and the data was analyzed by the use of the Winelli II software.[43]

2.2.2. Electron Microscopy. Transmission electron microscopy (TEM) characterization was performed in a Philips CM 200 electron microscope operating at 200 kV. The equipment works with a LaB$_6$ emission filament and is equipped with an

ultrathin objective lens. An EDS detector is attached to the microscope. The samples were prepared by scratching the thin films with a stainless steel chirurgical blade and depositing the scratched pieces over an ethanol drop placed on an ultrathin carbon film supported on a TEM Cu grid. Statistical counting of the particle size (on ca. 150–200 nanoparticles) was made on several micrographs to obtain the particle size distribution (PSD). It should be mentioned that this procedure, often reported in literature, gives an overestimated value of the mean particle size, since smaller particles are poorly defined and may be left aside in the counting. Field emission-scanning electron microscopy (FE-SEM) images were obtained with a ZEISS LEO 982 GEMINI field emission electron microscope in the secondary-electron mode, using an in-lens detector to improve resolution.

2.2.3. X-ray-Based Techniques. Film density was obtained from the analysis of the critical angle of X-ray Reflectometry (XRR) measurements that were performed at the D10A-XRD2 line of Laboratorio Nacional de Luz Sincrotron (LNLS), Campinas, SP, Brazil (λ = 1.5498 Å). In order to obtain accurate density values, measurements were done under dry nitrogen flux to avoid atmospheric water condensation within the pores which would lead to an underestimation of mesoporosity.[17] The same setup can be used to obtain a diffraction pattern in grazing incidence mode. Film mesostructure was analyzed using Small Angle X-ray Scattering (SAXS) in transmission mode at the D11A-SAXS2 line of LNLS (λ = 1.608 Å) at normal and 3° incidence on thin glass covers.

2.3. Modeling Scheme. The modeling framework of the Au@MTTF optical properties will be thoroughly presented and discussed in the next sections. Only a general sketch will be provided here. Effective Medium Approximations (EMA) were applied to the complex dielectric functions determined by ellipsometry for MTTF or Au@MTTF. Mie Theory was applied to the Au NP absorbance spectra obtained by UV–visible spectroscopy. From each independent model, the filling fraction (f_{NP}) and the NP radius (a) present in the NP@MTTF were calculated, as presented in Scheme 2.

**Scheme 2. Summary of the Modeling Applied to NP@MTTF System**
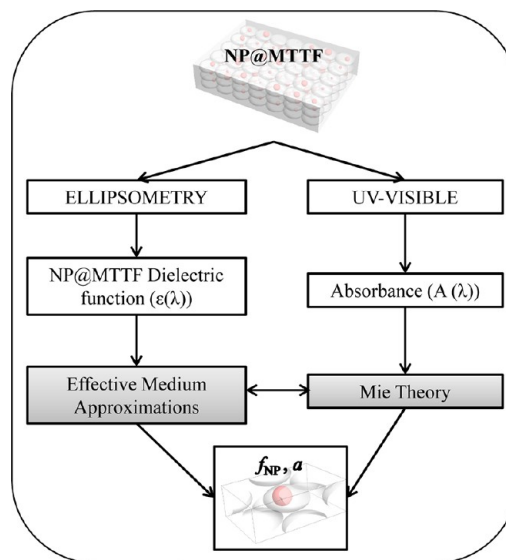
This procedure permits to obtain the pore filling fraction and the NP size by different models, and to evaluate their predictive power by confronting them to the crossed characterization techniques.

3. RESULTS AND DISCUSSION

3.1. Synthesis and Characterization of MTTF and Au@ MTTF nanocomposite films. *3.1.1. Mesoporous Thin Film Characterization.* The structure of MTTF deposited over soda-lime glass has been extensively characterized in several works[41] using different techniques including X-ray diffraction and scattering from synchrotron radiation (XRD, SAXS, XANES), high resolution TEM and dynamical thermo-ellipsometry characterization.[48] After thermal treatment at 350 °C, the film gets contracted by ca. 50% in the normal direction relative to the substrate, the oxide framework being mainly amorphous but containing a partially crystalline (ca. 20%) anatase phase.[49,50] Under the thermal treatment conditions employed in this work, highly ordered, mostly amorphous MTTF with similar pore size are obtained. The structure of the films can be described through their thickness, porous volume fraction, pore size, interpore distance, and the characteristic size of the channels or necks connecting adjacent pores. While the interpore distance calculated from SAXS at normal incidence was found to be (11.9 ± 0.3) nm for the systems analyzed in this work, the thickness was determined by both ellipsometry and XRR, obtaining a coincident value of (120 ± 10) nm. EP measurements reveal a type IV adsorption isotherm with a H2 hysteresis loop, which is characteristic of a porous system composed of discrete pores with necks or restrictions.[51] The total accessible volume reaches 45% and, from the adsorption and desorption branches respectively, a pore size of (10 ± 3) nm and a neck size of (6 ± 1) nm could be estimated. SAXS measurements at 3° incidence reveal that the titania films present a contracted $Im\bar{3}m$ mesophase with long-range pore order. Details of the characterization of the MTTF are shown in the Supporting Information (SI).

3.1.2. Characterization of Nanoparticles Embedded in MTTF. Gold nanoparticles were grown into the MTTF pores as detailed in the Experimental Section. Figure 1 shows the absorbance spectra obtained as the number of reduction steps (RS) was increased. It is possible to observe that the gold LSPR position keeps practically invariant for 1 to 10 reduction steps, while its peak position shifts slightly to higher wavelengths for a higher number of RS (Figure 1, inset). This shift in the plasmon position might be due to interparticle interactions, due to the nucleation of new Au NP, or to the growth of adjacent NP. It is known that for interparticle distances similar to the NP diameter, plasmons might interact with each other leading to a red shift in the LSPR.[52,53] These interactions seem to take place for films submitted to more than 10 reduction steps. Therefore, under the conditions of synthesis presented in this work, only NP produced in less than 10 RS can be safely considered to be isolated from each other. Thus, in order to develop an appropriate description of the LSPR of gold NP infiltrated inside the MTTF neglecting the interparticle interactions, attention will be focused on films submitted to five reduction steps (5 RS). Figure 2 shows TEM images of MTTF film before and after 5 RS. The use of TEM to determine NP distribution, sizes, and the degree of interparticle connection is widely spread out in the literature.[33,34,54−57] In our case, Figure 2 shows that NP present mostly an isotropic shape, that could be in principle considered as spherical, and
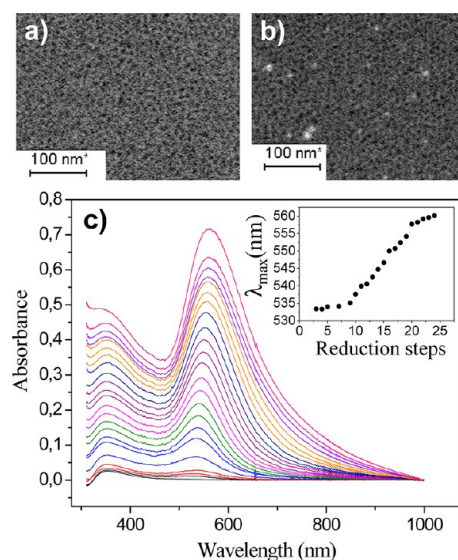
Figure 1. FE-SEM images of the MTTF before (a) and after (b) gold infiltration. (c) Absorption spectrum of the nanocomposite showing the evolution of the LSPR band after each reduction step of $AuCl_4^-$. The shift in the LSPR peak position at increasing loadings is shown in the inset.
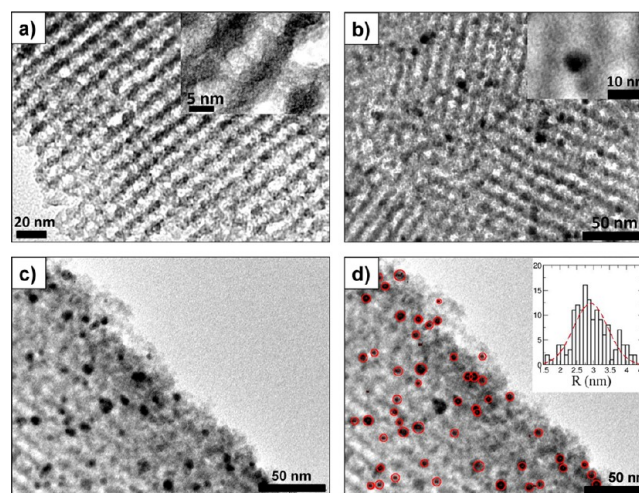
Figure 2. TEM images of mesoporous TiO_2 thin films before (a) and after (b, c) the infiltration with gold NP through five reduction steps (5 RS). In image (d), an example is shown of the particle statistical counting of image (c), displaying the PSD obtained by computing nanoparticle size from different TEM images in the inset.

are sufficiently isolated to consider the absence of interactions among them. The occupied pore volume fraction was characterized by EDS and XRR techniques (see SI for details), resulting in a filling fraction of the porous volume of 1.9% and 2.2%, respectively. Figure 2d shows the NP size distribution analysis carried out over several TEM images, where it is possible to determine a distribution with an average radius $a = (2.9 \pm 0.5)$ nm.

3.2. Modeling Framework. In order to model the optical response of NP@MTTF, it is first necessary to define how the NP and the MTTF are themselves represented. Then, the description of NP@MTTF and its subsequent comparison with experimental results can be attempted.

3.2.1. Mesoporous Titania Thin Films (MTTF). The modeling of MTTF is performed at optical frequencies,

consequently the incident wavelength used (350−900 nm) is much larger than the pore size. Therefore the MTTF can be considered as an homogeneous effective medium. Several works describe porous materials through effective medium approximations (EMA)[52] in which the material refractive index is expressed as an effective value, in this case: n_{MTTF}. This quantity can be calculated by using a mixing rule of the refractive indexes of the different components that constitute the material. In particular, the MTTF effective medium is composed of the mixture of the refractive indexes of dense titania and of air—inside porosity.

A comparison between different EMA models to describe the dielectric function of highly ordered mesoporous thin films has been recently addressed by Hutchinson and co-workers;[58] they concluded that the employment of the Asymmetric Brugge-man[59] (AB) model leads to the most accurate description. Based on this conclusion, we applied the AB model given by the following expression:

$$1 - f_p = \frac{\left(\frac{n_{MTTF}^2}{n_{ds}^2} - \frac{n_{air}^2}{n_{ds}^2}\right)}{\left(\frac{n_{MTTF}^2}{n_{ds}^2}\right)^{\frac{1}{3}} \left(1 - \frac{n_{air}^2}{n_{ds}^2}\right)} \tag{3}$$

where f_p denotes the volume porous fraction, n_{MTTF} the porous material effective refractive index, n_{air} the air refractive index ($n_{air} = 1$) and n_{ds} the refractive index of the wall, i.e., the dense solid, at a given wavelength.

SE characterization was carried out at 0% of relative humidity (RH) to determine the optical constants of MTTF and also of dense titania films prepared according to the protocols presented in the Experimental Section. With this information, eq 3 was used to calculate the MTTF effective refractive index (n_{MTTF}) and the porous volume fraction (f_p) employing $n_{air} = 1$ and n_{ds} as the dense titania refractive index acquired by ellipsometry. The resulting values of n_{MTTF} were compared to the direct determination of the MTTF dielectric function through SE. According to the model, the n_{MTTF}, a total porous volume $f_p = 0.42$ was calculated, which is in close agreement with the experimental value of $f_p = 0.45$ directly measured by EP.With these results, we conclude that the use of asymmetric Bruggeman model is adequate to represent the MTTF medium as shown in Figure 3. Consequently, the concept of MTTF as an effective medium is valid, and it is well characterized by both the ellipsometric measurement and the numerical calculus.

3.2.2. Nanoparticles. The interaction of metallic NP with light leads to the appearance of LSPR.[60−65] LSPR depends on the metallic compound as well as on NP features such as morphology,[66,67] size, interparticle interactions,[11] and on the
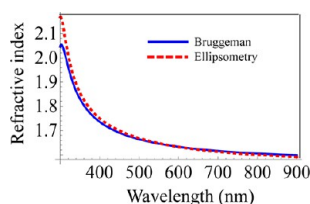
Figure 3. Comparison of the dispersion relation of the refractive index achieved after the fitting of the ellipsometric data obtained directly from the measurement of the mesoporous thin film with the result of the asymmetric Bruggeman EMT calculation for the mixture of dense TiO₂ thin film and air in a volume fraction of 0.42.

refractive index of the surrounding medium.[38,52,65] In the context of Mie Theory, NP can either absorb or scatter light, defining the extinction coefficient ($c_{extinction} = c_{absorption} + c_{scattering}$).

For spherical NP below 10 nm in size, the *quasi-static approximation* is valid, and the scattering coefficient is negligible in comparison with the absorption coefficient. It is also possible to account only for the dipolar mode—*dipolar approximation*—and consequently, the LSPR frequency does not depend on the NP size—for spherical NPs between 2 and 10 nm.[52,56,60,64,65]

The optical properties observed for metallic compounds arise from the response of their electronic structure to the electromagnetic field—provided by light source. Although the dielectric function of metallic NPs cannot be measured directly, it is feasible to describe it considering the NPs' electronic structure. Two types of electrons can in principle be distinguished in the simplest model: bonded and free—i.e., conduction—electrons. While free electrons provide the major response of the NP to the electromagnetic field, and are responsible for NP polarizability, bound electrons will also exert an influence:

$$\varepsilon(\omega) = \varepsilon_{e-bound}(\omega) + \varepsilon_{e-free}(\omega) \tag{4}$$

Several expressions for the dielectric function corrected to account for the reduce size of the particles are addressed in literature,[11,61,68−70] being the dielectric function reported by Hövel et al.[71] the one employed in this work:

$$\varepsilon(\omega, r, A) = \varepsilon_{bulk}(\omega) + \frac{\omega_p^2}{\omega^2 + i\omega\gamma_M}$$
$$- \frac{\omega_p^2}{\omega^2 + i\omega(\gamma_M + \gamma(a, A))} \tag{5}$$

We selected this function because it constitutes a full description of the NP dielectric function where NP size, NP interface, and also bound electrons are considered, as explained below.

In eq 5, Drude's model is employed to describe free electrons in a metal, where ω_p is the plasma frequency (1.37×10^{16} s⁻¹) and γ_M (3.18×10^{13} s⁻¹) is a phenomenological parameter that represents the macroscopic damping constant due to the dispersion of the electrons by the ions of the *bulk* material. For NPs with smaller size than the mean free path of conduction electrons,[57] an additional term is added to the damping constant:

$$\gamma(a, A) = Av_F/a \tag{6}$$

This term accounts for interface dispersion damping—v_F indicates the Fermi velocity (1.41×10^{16} m·s⁻¹) and a the NP radius—as it considers the effect of the NP/medium interface on the conduction electrons through the A parameter. The value of A depends on the theory employed to calculate it and it is usually around 1.[70,72] As A represents the effect of the interface characteristics into the NP dielectric function, this value depends on the contact angle of the NP with the oxide walls of the MTTF. According to Hilger et al.,[73] the A parameter for silver NP varies from 0.6 to 1.8, from NP in vacuum to NP totally immersed in a titania matrix. We expect similar values for Au NP also immersed in titania.

Dielectric functions for bulk (ε_{bulk}) materials such as silver and gold have been reported in works of Palik[74] and Johnson and Christy.[75] The use of each of the dielectric functions

7250

dx.doi.org/10.1021/jp3127847 | J. Phys. Chem. C 2013, 117, 7246−7259

depends on the spectral range in which calculations are carried out. For optical frequencies such as those studied here, the Johnson and Christy data were found to be more accurate.

3.2.3. Nanoparticles Immersed in MTTF. In the context of Mie theory, NP absorption coefficient within the dipolar approximation is well-defined for isolated particles of radius a by:[76]

$$C_{abs}(a, A, \omega) = 4\pi k a^3 \text{Im}\left[\frac{\varepsilon_{NP}(a, A, \omega) - \varepsilon_{MTTF}(\omega)}{\varepsilon_{NP}(a, A, \omega) + 2\varepsilon_{MTTF}(\omega)}\right] \quad (7)$$

Equation 7 describes the absorption coefficient expression per NP, where $k = 2\pi/\lambda$, ε_{NP} the NP dielectric function, and ε_{MTTF} the medium dielectric function.

From eq 7, the absorbance can be obtained considering the number of NP per unit area (N_{NP}) present in the sample:

$$\text{Abs}(a, A, \omega) = N_{NP} C_{abs}(a, A, \omega)/\ln(10) \quad (8)$$

where Abs represents the absorbance measured in normal transmission mode in an UV–visible spectroscopy experiment.

From eqs 7 and 8, it is possible to observe that Abs depends on the number N_{NP}, on NP size (a), on NP/MTTF interface (A), and on the medium dielectric constant $\varepsilon_{MTTF}(\omega)$.

It is known that the Abs function can be directly compared with the UV–visible spectrum of the sample in order to fit its function parameters. It is worth to mention that only two set of parameters can be determined together: a and N_{NP} or A and N_{NP}, the $\varepsilon_{MTTF}(\omega)$ corresponds to the dielectric function determined through eq 2 by the n_{MTTF} value acquired from the ellipsometric measurements (eq 3).

Taking this into account, we first employed the absorbance spectrum of a sample with a well-known NP radius (a) acquired from TEM measurements—see Figure 2—in order to obtain the A and N_{NP} by fitting the Abs function to the experimental spectrum. The A parameter thus determined can then be employed to describe the effect of the interface between Au NP and MTTF.

Once the A parameter is known, another sample can be taken and by fitting the Abs function to its UV–visible spectrum, the NP radius (a) and the N_{NP} can be determined.

Besides that, in a unit area, N_{NP} can be related to the pore volume fraction occupied by the NP (f_{NP}), to the pore volume fraction (f_p) of the film, to the NP radius (a) and also to the film thickness (d) by the following,

$$N_{NP} = \frac{3 f_{NP} f_p d}{4\pi a^3} \quad (9)$$

However, NP inside MTTF can be modeled through an EMA approach where n_{eff} and k_{eff} represent the NP@MTTF refractive index. This effective refractive index is obtained by combination of MTTF dielectric function—measured by ellipsometry—and metallic NP dielectric function—eq 5. The Maxwell–Garnett (MG) model[37] is an EMA that describes metallic spherical inclusions into an homogeneous matrix,

$$\frac{\varepsilon_{eff} - \varepsilon_{MTTF}}{\varepsilon_{eff} + 2\varepsilon_{MTTF}} = f_{NP} f_p \frac{\varepsilon_{NP} - \varepsilon_{MTTF}}{\varepsilon_{NP} + 2\varepsilon_{MTTF}} \quad (10)$$

where ε_{eff} is the NP@MTTF dielectric function, ε_{MTTF} the MTTF dielectric function, ε_{NP} the NP dielectric function, f_p the porous fraction, and f_{NP} the NP volume fraction. If NPs are spherical and do not interact with each other, then MG and

Mie theory should lead to the same results: a and f_{NP}, considering that A is known.

Besides the modeling through UV–visible spectra, it is also possible to obtain the dielectric constant of the NP@MTTF system by ellipsometry. This function can be used to determine the absorption coefficient (see eq 2), from where the absorption constant (γ_{abs}) can be calculated:

$$\gamma_{abs}(a, A, \omega) = 4\pi\kappa/\lambda \quad (11)$$

which is an intrinsic optical property of the film that can be converted into its absorption spectra by the following:

$$\text{Abs}(a, A, \omega) = \gamma_{abs} d/\ln(10) \quad (12)$$

where d denotes the film thickness.

From eq 2, 11, and 12, the dielectric function can be transformed into the absorption spectra.

In particular, we used this strategy to transform the ε_{eff} obtained from MG theory to UV–visible spectra and compare it with experiments and Mie's theory results. This can also be applied to convert ε_{eff} measured by ellipsometry into UV–visible spectrum. Figure 4 displays α and β angles [that are related to the Δ and Ψ parameters of an SE measurement. (They are related by the following: $\cos\Delta = (\beta/(1 - \alpha^2)^{1/2})$,
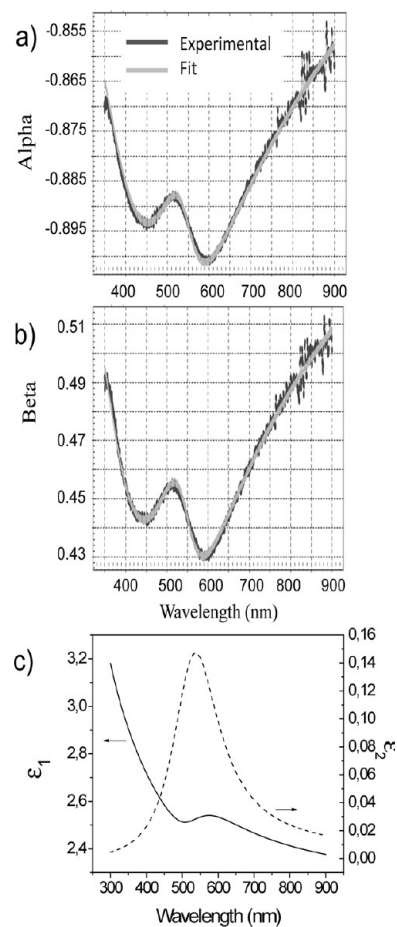

Figure 4. Ellipsometric functions Alpha (a) and Beta (b) for the TiO$_2$–Au5RS sample. The result of the fitting of the proposed model is presented superimposed (gray curve). In (c), the reconstruction of the dielectric function for both the real (ε_1) and imaginary (ε_2-dashed line) components is shown, obtained from the fitted parameters of the model.

tanψ = $((1 + \alpha)/(1 - \alpha))^{1/2}$ tan A, where A is the analyzer angle, 45° in our case)], with their corresponding fitting and the dielectric constant obtained for Au@TiO$_2$.

3.2.4. Au@TiO$_2$: Comparison between Modeling and Experiments. Two different samples of Au@TiO$_2$-5RS—obtained after 5 reduction steps—were considered. From the analysis of the TEM images, an average radius a of (2.9 $\pm$ 0.5) nm is extracted (Figure 3), and employed in eq 8 to determine the Abs parameters (A and N_{NP}) by fitting this function to the absorbance spectrum. As a result we calculated an A value of 1.5, which is representative for this kind of system: Au@MTTF. This result for A value could be expected in analogy to the increase in the A parameter with respect to the vacuum value reported for Ag NP in contact with TiO$_2$.[73]

Once the A parameter was set up as 1.5, we determined on the other Au@TiO$_2$-5RS sample the radius a and the filling fraction f_{NP}, by using Mie (eqs 8 and 9) and MG (eqs 2, 11, and 12) theories. Results are addressed in Figure 5, with the
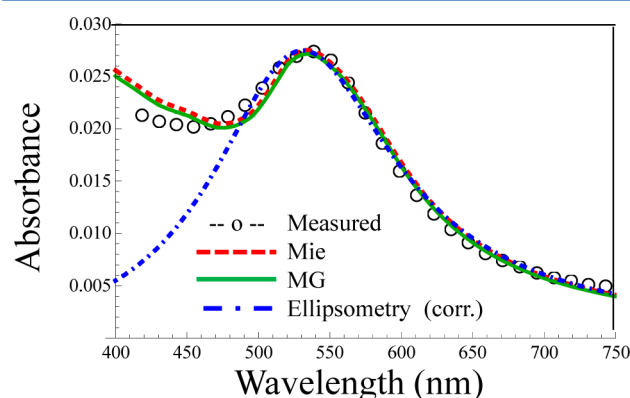
Figure 5. Experimental (circles) and calculated absorbance spectra of Au5RS sample performed through Mie theory (red, dashed) and Maxwell−Garnett EMT (green, solid). Comparison with normalized spectra calculated from the parametrized effective dielectric function obtained from ellipsometry measurements (blue, dashed).

corresponding correlation function for the adjustment with respect to the UV−visible spectrum within the range of 440 to 750 nm. The Abs functions determined by both models are also displayed in Figure 5, from which it can be observed an excellent coincidence between the experimental spectrum and the models.

The effective dielectric function (ε_{eff}) of Au@TiO$_2$-5RS was obtained not only by MG modeling (eq 10) but also by ellipsometry (Figure 4). Using eq 2 and eqs 11-12 it is was possible to determine the absorbance spectrum from the ellipsometry measurement. The LSPR peak position as well as the plasmon width can be reproduced by the ellipsometry data when it is converted to the absorbance spectrum. Regarding the LSPR intensity, which is related to the absolute absorbance value, in our case is overestimated—by a factor of 2—by this technique. For this reason, the corrected spectrum is shown in Figure 5. A more detailed discussion about the excellent correspondence of these two techniques for adsorbed dye molecules can be found in the SI.

Once the corrected spectrum is obtained from ellipsometry, we can determine by MG theory (eqs 2, 10−12)—as we did for UV−visible spectrum—the NP size and f_{NP}. The results obtained from these two techniques are in accordance (see Table 1).

Table 1. Fitted Parameters a and f_{NP} for MG and Mie Theories with Respect to UV-Visible Spectra along with the Correlation Function R^2 Obtained for Each Adjustment

$A = 1.5$	f_{NP} (%)	a (nm)	R^2
Mie vs UV	1.77	2.88	0.99
MG vs UV	1.76	2.89	0.99
MG vs ellip. (corr)	1.78	2.87	0.99

It is useful to remark that the ellipsometric ε_{eff} of Au@TiO$_2$-5RS is constructed by Cauchy and Lorentz models within the range of 400−960 nm. The Lorentz model accounts for LSPR, leading to an adsorption coefficient that only corresponds to the LSPR. As no term is added to model the Au NP interband transitions, the spectrum obtained at shorter wavelengths—around 400 nm—is different than the ones determined by Mie and MG models as well as the one acquired by UV−visible spectrophotometer. It can be seen, Figure 5, that the Au interband transitions are far enough of the LSPR. Therefore, its influence should be minor, and for this reason we believe it is not relevant to account for the interband transitions in the ellipsometric measurements.

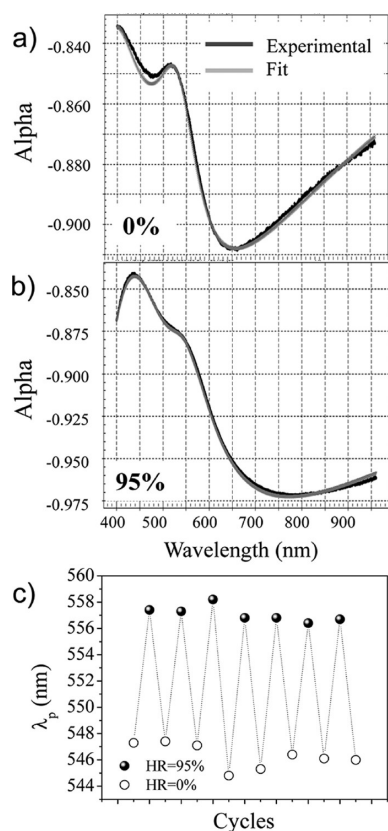For this case, the average gap distance (d_{gap}) can be estimated as follows:

$$d_{gap} = (3f_p \text{d}/4\pi N_{NP})^{1/3} - 2a \qquad (13)$$

Considering the NP inside the porous volume fraction of the MTTF, an average value of gap distance d_{gap} =12.0 nm (defined between NP surfaces) is obtained for 5RS . This value, which is slightly higher than the interpore distance, supports the idea of noninteracting NP, individually located in the mesopores.

3.3. The Effect of the Relative Humidity. Due to the high surface area and the presence of mesopores, exposure to increasing vapor pressure of a solvent, such as water, leads to adsorption on the MTTF pore system. A gradual increase of the refractive index is observed for low RH values since the onset of water capillary condensation takes place for RH values in the range 55−65% (see EP results in Figure S1 of the SI). Upon condensation of water inside the pores, a dramatic change in the effective refractive index is observed, if compared to the minor change (between 1.53 and 1.55) observed for values below the critical vapor pressure of condensation. This allows the employment of two components to describe the Au@MTTF system even though experiments are carried out in ambient conditions, where RH < 45%.
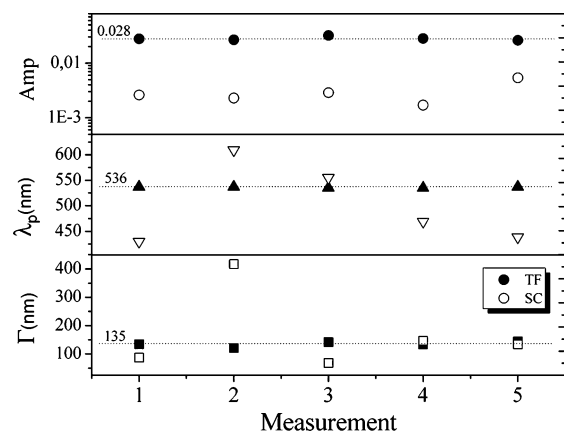
Since the pores and the NP present in the film are accessible to the humidity, capillary condensation of water leads to a plasmonic response.[21,77] With the aim of studying this effect, we characterized the LSPR at 0% and 95% RH by SE, obtaining an excellent agreement between the proposed model and the measurements (Figure 6). The plasmon position recorded for successive measurements under these two conditions show a reproducible and reversible 10 nm bathochromic shift of the LSPR peak position, as shown in Figure 6c. It is noteworthy to observe that the peak positions in "dry" and "wet" conditions do not suffer an appreciable shift or trend under the explored conditions (7 cycles), demonstrating the robustness of this nanocomposite system.

3.4. Bilayer Systems. In order to analyze the extension of the method proposed. we synthesized a bilayer mesoporous system composed by two mesoporous thin films, SiO$_2$-CTAB (SC) and TiO$_2$-F127 (TF), as described in the Experimental Section. The sample consists of a CTAB-templated silica (SC)
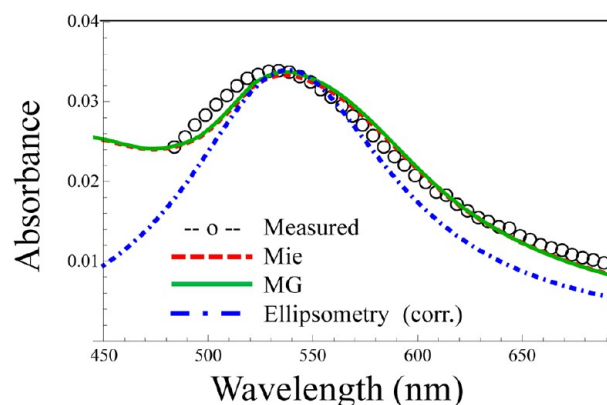
Figure 7. Fitted parameters describing the amplitude, peak position, and broadness of the Lorentz function of the LSPR for each layer in Au10RS-TF/SC/glass.

Figure 6. Ellipsometry measurements at different RH conditions. Parts (a) and (b) show the alpha values at 0% and 95% RH, respectively. The shift in LPSR peak position upon exposure to cycles of 0% and 95% RH is displayed in part (c).

adsorbed within the titania mesopores, in which the iep is in the ∼5−7 range. Additionally, the selective reduction might be catalyzed by TiO_2 as was reported to occur in bilayer mesoporous thin films for the case of silver NP.[17]

For the calculation of the particle size and the filling fraction, the porous volume fraction of the TF layer was determined through EP in the bilayer system; a value of 35% pore volume was found.

As in the case of the monolayer TF sample, and using the previously discussed value of $A = 1.5$, the fitting procedure of the Mie and Maxwell−Garnett calculated spectra was performed to the measured absorbance of the Au10RS-TF/SC sample. The results are displayed on Figure 8, together with

layer in contact with the substrate (glass) while the upper layer is an F127-templated titania (TF), as described in ref 44. For the ellipsometry measurements, each layer was adequately adjusted through a Cauchy model. This bilayer system was infiltrated with Au NP with 10 reduction steps (10RS) since the LSPR developed after each RS was found to be less intense than for the monolayer system. The sample was measured using microspot SE (<1 mm beam diameter) in five different points separated several millimeters from each other. The measurements were analyzed proposing a model in which a Lorentz oscillator was added to the dielectric description of each layer to account for the LSPR. The starting parameters for this absorption component were exactly the same for both layers, i.e., the same filling fraction of Au NP was supposed as a starting point in the fitting procedure. The parameters describing the LSPR for the TF layer converged in all cases to similar values, while the ones corresponding to the SC layer were more erratic (Figure 7); in particular, the amplitude of the Lorentz functions in this case were 1 order of magnitude less than for the TF layer, suggesting a significantly lower filling fraction for the SC layer. In fact, the fitting of a model that accounts for NP only in the TF layer (no Lorentz function added to SC dielectric function) was excellent ($R^2 = 0.996$). These results strongly suggest that the infiltration-reduction procedure is taking place mostly at the TF layer, and much less in the SC layer. This can be explained by considering the low adsorption of $AuCl_4^-$ anions at pH 4 in SiO_2, in which the isoelectric point (iep) is close to ∼2, as previously reported.[78] On the contrary, the Au(III) precursor can be efficiently


Figure 8. Experimental (circles) and calculated absorbance spectra of Au10RS-TF/SC sample performed through Mie theory (red, dashed) and Maxwell−Garnett EMT (green, solid). Comparison with normalized spectra calculated from the parametrized effective dielectric function obtained from ellipsometry measurements (blue, dashed).

the corrected spectra calculated from the ellipsometry measurement. From the analysis of the spectra, a particle radius $a = (2.8 ± 0.1)$ nm and filling fraction $f_{NP} = (3.8 ± 0.1)$% of the porosity can be extracted.

3.5. Analysis of NP Growth. The model developed in this work can be applied to the first ten reduction steps in order to shed light into the infiltration mechanism. We determined NP radius and f_{NP} for five different reduction steps (4 to 8 RS) through modeling their plasmonic response. From these results, we calculated the number of NP per volume unit
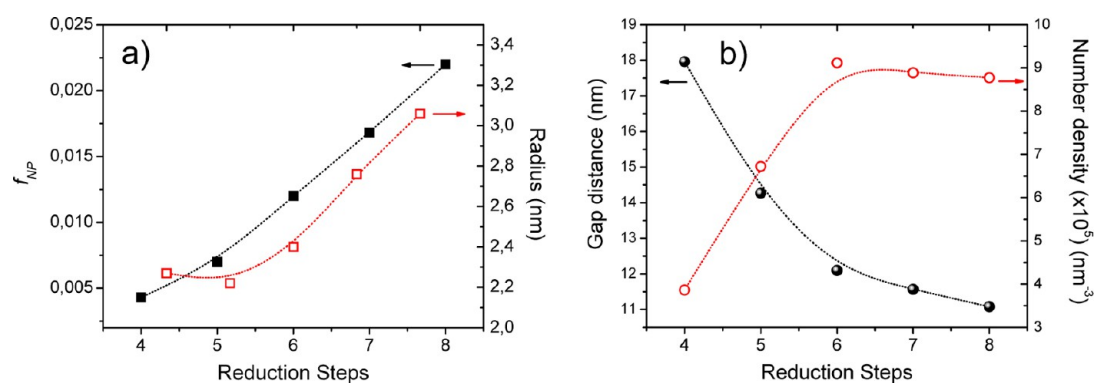
Figure 9. Calculated values of (a) filling fraction and particle radius and (b) average gap distance (d_{gap}) and particle density ($N_{NP}{}^{v}$) after successive reduction steps.
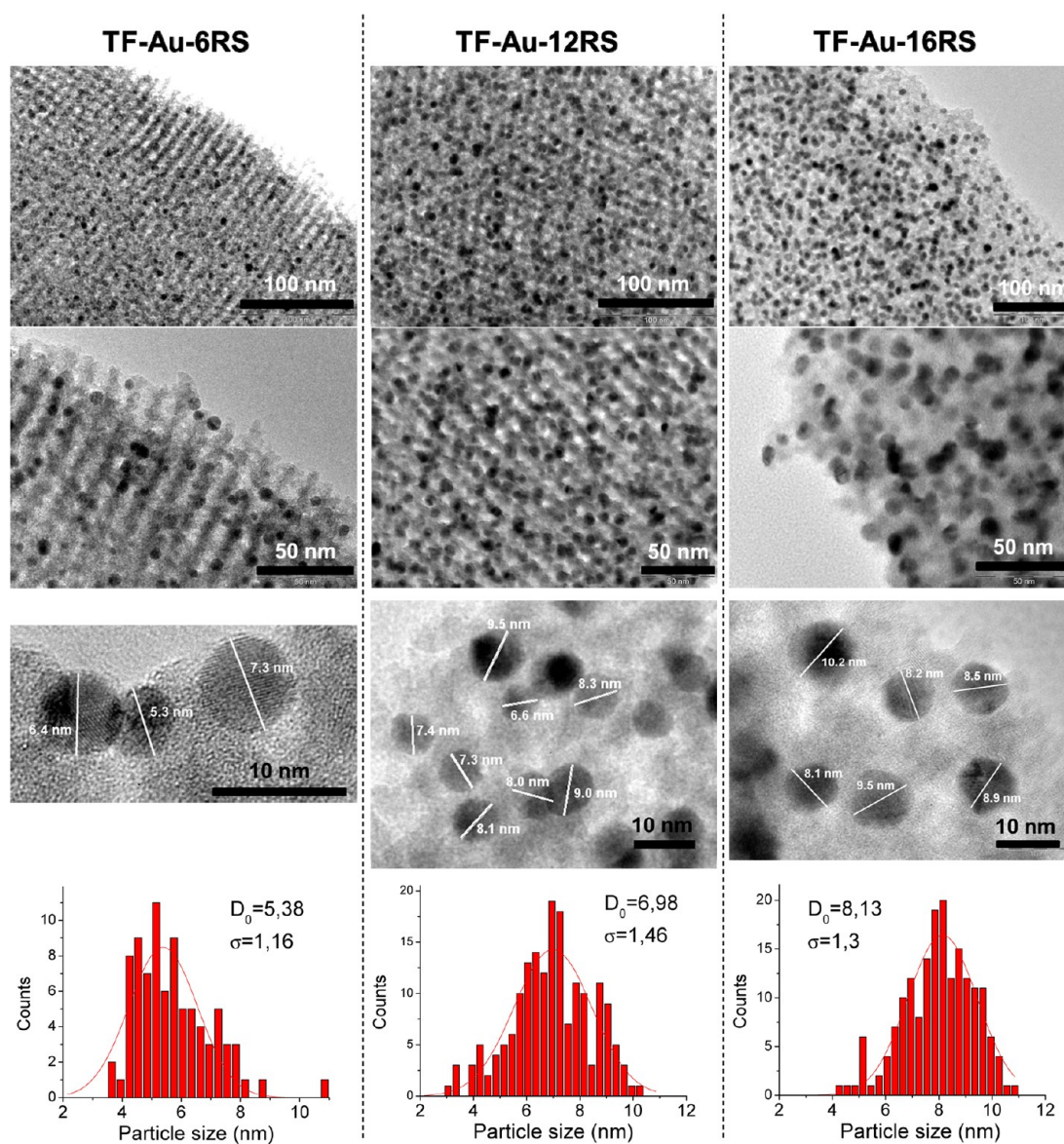
Figure 10. TEM images of MTTF filled with Au NP after 6, 12, and 16 reduction steps, and statistical counting of several images (mean particle size (D_0) and standard deviation (σ) determined from Gaussian fits in each case).

($N_{NP}{}^{v} = N_{NP}/d$) and the interparticle gap distance (d_{gap}, eq 13). We observed that both $N_{NP}{}^{v}$ and NP size increase during the infiltration, but $N_{NP}{}^{v}$ reaches a plateau after the sixth reduction step, as shown in Figure 9. In addition, the calculated d_{gap} exhibits a decreasing trend for subsequent reduction steps.
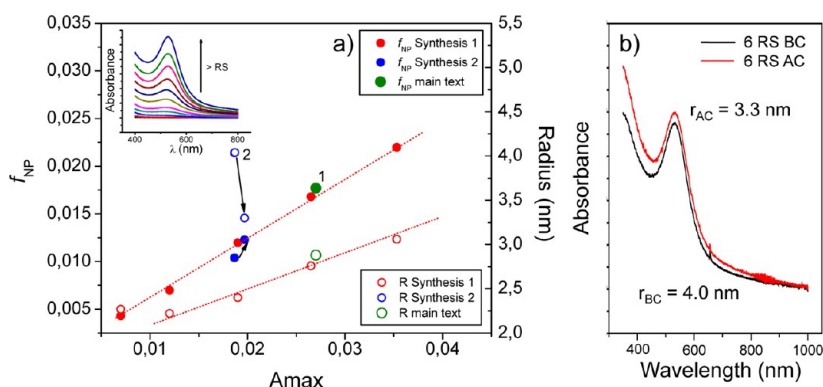
Figure 11. (a) Calculated values of filling fraction and particle radius for two different samples prepared in similar conditions. The inset shows the evolution of the spectra for synthesis 1. The point marked as 1 represents the monolayer sample discussed in Section 2. The point marked as 2 corresponds to the particle radius and filling fraction calculated before and after cleaning the film surface. In panel (b) spectra of sample referred as 2 before cleaning (BC) and after cleaning (AC) the film surface with their respective calculated radius.

The observed behavior suggests that the mechanism of particle formation proceeds through nucleation and growth. A fast nucleation and growth of ca. 2 nm radius particles takes place in the first steps; subsequent exposure to Au(III) precursor and reducing agent can lead to concurrent nucleation and growth processes. After six reduction steps, however, while the NP filled pore volume and NP size keep growing (Figure 9a), the total number of nanoparticles (N_{NP}^v) levels off, suggesting that nanoparticle growth dominates the scenario, and new nucleation is no longer significant. The NP radius increase is accompanied by a significant decrease in the interparticle gap distances (Figure 9b).

It is interesting to note that calculated gap distances are smaller than the pore diameter, i.e., each pore contains one metallic nanoparticle at most, which is also consistent with the TEM observations. In the RS < 10 regime, thus, the presented model of isolated spherical nanoparticles is valid, and useful information on nanoparticle size, separation and pore filling can be simultaneously extracted. Plus, this method permits to shed light into a crucial question: which should be the effect of the number of nuclei or NP size in the shape of the plasmon.

For further infiltration-reduction cycles, the situation is more complex. As observed in Figure 1C, a significant bathochromic plasmon shift takes place for RS > 10. Figure 10 shows TEM micrographs of MTTF exposed to 6, 12, and 16 RS. A higher number of larger size particles are obtained within the pore systems after successive RS. A thorough statistical analysis performed on top-view micrographs permitted to determine an increase in the NP horizontal section from ca. 5 nm to almost 9 nm while going from 6 to 16 RS. In the latter case, completely filled mesopores are observed, as well as patches of neighboring nanoparticles of similar size.

The observed optical and structural properties can be due in principle to the combination of three effects that take place for RS > 10:

(a) Nanoparticle size growth;
(b) Development of nanoparticle asymmetry; and
(c) Plasmon coupling between nanoparticles.

In this context, we can advance that the mechanism of NP growth within the pore system is complex, and implies the steps a-c presented above. For low pore fillings, almost spherical nanoparticles grow and the model adequately describes them. For higher Au pore filling, nanoparticle growth is responsible of the increase in the plasmon absorption. Further growth can lead to full pore filling, leading to ellipsoidal nanoparticles and eventually to pore blocking.[79] In the latter case, Au° nucleation can take place at the TiO₂−solution interface of an empty pore. In the high supersaturation conditions present in this reduction method, new nucleation is likely followed by very fast nanoparticle growth. This leads to a leveling off of the NP size, which is ultimately templated by the pore size and shape. In addition, for RS > 10, NP sizes begin to be comparable to gap distances (see Figures 9 and 10), implying optical interaction between NP, sustaining hypothesis (c). In summary, the combined interplay of NP shape and interactions can explain the steep red shift in the spectra for RS > 10 presented in Figure 1.

The model framework presented here accounts for spherical NP between 2 and 10 nm without interactions, but could be extended to other shapes and sizes. It could be easily employed for ellipsoidal NP through the use of Gans theory as an extension of Mie's and the EMA model given by Polder and Von Santen.[80] For NP larger than 10 nm, the dipolar approximation is no more valid, and higher modes have to be considered for the extinction coefficient C_{ext}. Consequently, the model can be extended to these systems but at the expense of increasing the computing time. It is worth mentioning that this way of modeling the LSPR of gold NP included in MTTF can be extended either to other matrix systems, such silica and zirconia mesoporous thin films, or to other metallic NP, such as Ag NP. As the A parameter is intrinsic of each composite it has to be determined for each case.

The main limitation, however, arises when interparticle distances become short enough for electromagnetic interactions to take place. In such a scenario, MG and Mie theories are no longer valid, and more complex calculation methods should be applied,[11] in particular García and co-workers presented a simple way to account for the interactions by the addition of a single extra parameter.[81]

3.6. Critical Aspects Concerning Reproducibility and Predictive Power. The model presented here permits to extract NP size, particle density, pore filling fractions, and mean gap distance for gold NP embedded within a mesoporous matrix from the analysis of LSPR bands. This information also permits us to understand the formation paths of such nanocomposite systems, opening the possibility to design their optical properties.

The reproducibility of the reduction process that leads to NP generation is a very important issue. We noticed that the

spectra of independent experiments presented slight differences on the maximum absorbance along the reduction steps. Consequently, we decided to compare these sets by classifying them by their maximum absorbance, instead of considering the number of reduction steps performed.

Figure 11a shows the calculated filling fraction (f_{NP}, closed red symbols) and NP radius (open red symbols) of a series of reduced samples presented in Figure 9, replotted as a function of the absorbance maximum. The increasing trend regarding both quantities along reduction is still evident. An excellent agreement between the NP size and pore filling of this series extracted from the modeling of the optical properties and the independently obtained sample discussed in Section 2 is presented in Figure 11a. This reinforces the confidence in the predictive capacity of the model.

However, there are subtleties in the synthesis method that have to be taken into account in order to make a correct evaluation of the system properties obtained from the spectra. An independent experiment performed in slightly different conditions, named synthesis-2 (Figure 11a, blue symbols) exhibits a similar filling fraction to synthesis-1, but a greater NP radius. The only difference between these two syntheses is the cleaning procedure of the film surface. On synthesis-1, the film surface was cleaned after each reduction step before measuring its spectrum, as was done in the film thoroughly discussed in Section 2. This cleaning step after each RS was not performed for synthesis-2. To study this effect on synthesis-2, we cleaned the film surface and measure its spectra immediately after (see Figure 11b) and recalculated the filling fraction and radius, obtaining a substantial difference on the radius determined. The average NP radius obtained after cleaning the film surface was in very good agreement with TEM images of this sample (6 ± 1 nm diameter, Figure S8 SI). Observing the slight difference between spectra, Figure 11b, and the clear difference on the subsequent radius determined, Figure 11a, we observe that this modeling methodology detects subtle variances on the particle growth among sets of experiments that would be difficult to assess by other characterization techniques. We believe that the first infiltration-reduction steps are more sensitive to physicochemical conditions that affect the NP growth mechanism, including synthesis variables that were not systematically explored, such as temperature, film thickness, and the aging of Au(III) and $NaBH_4$ solutions. As demonstrated above, the cleaning process before infiltration is also important. However, we have to remark that the modeling of the plasmon response developed in this work provides a very sensitive tool to observe and eventually correct the influence of these conditions in the actual synthesis.

3.7. Discussion. We understand that ellipsometry possesses several advantages in the task of characterizing the LSPR of an optical material such as NP@MTTF. SE opens the possibility to study the LSPR at different relative humidity (i.e., EP), as well as providing structural information such as the localization of the NP in a multilayer MTTF, or even in a more complex nanostructure involving both NP and adsorbed dyes (see Figure S7 of the SI), which is applicable to dye-sensitized solar cells (DSSC). EP allows the evaluation of the plasmon response of the nanocomposite material to changes in environment vapor pressure, providing an additional tool in the research of these materials acting as vapor sensors. For the bilayer system analyzed in this work, the nanostructural information regarding the localization of NP could only be achieved by more complex characterization techniques such as high resolution electron

microscopy, (e.g., TEM in cross section mode), Rutherford backscattering (RBS) or XRR. Ellipsometry, in this sense, provides a nondestructive optical option for this sort of studies. However, the limitation of the technique must also be considered both in the conditions of the measurement itself and on the accuracy of the resulting parameters after the fitting. The former issue involves: the ambient conditions in the surroundings of the sample, the angle of incidence which must be as close as possible to the Brewster angle, and the use, or not, of a microspot configuration. Since the use of a microspot reduces the area of measurement to a few hundreds of square micrometers, increasing the intensity of the signal, several points of the sample should be acquired in order to quantify its homogeneity and the statistical standard deviation of the fitted parameters. This analysis depends, of course, on the particular sample under study, but the inhomogeneity could possibly be the principal source of incertitude in the resulting values, regardless of the accuracy of the fitting. With respect to the fitting procedure, several topics emerge: on one side, the dielectric model proposed could only be applicable to a restricted range of the spectrum, as in this case, limiting the validity of the resulting dielectric functions outside the fitting range. However, once the model and the multilayer structure are selected, the fitting procedure is highly dependent on the starting parameters as the minimization has not a unique solution. For this reason, any previous information of the sample is valuable and careful must be taken for the analysis of unknown samples.

Alternatively, regardless of the simplicity of its operation, spectrophotometry provided direct and confident information about the absorbance spectrum for the sort of samples analyzed in this work. Although nontransparent substrates could also be analyzed in a similar way in reflectance mode, it requires special accessories, like optical fiber systems or integration spheres, of less common accessibility. In any case, the spectrum acquired is insensitive to the details of the micro/nanostructure of the sample since it only relates the intensities of the incoming and outgoing light and no extra information is retrieved regarding the phase and polarization of light. As was shown in this work, the absorbance spectra obtained for the samples studied is sufficient to calculate both the volume filling fraction and the mean radius of the NP present in the MTTF, but it fails to provide additional information about the microstructure like the location of the NP in a mesoporous multilayer film.

We would like to remark that the employ of TEM images is decisive to determine the NP morphology and size. The feedback between TEM images and the optical techniques (UV−vis spectroscopy, ellipsometry) permitted to determine the A parameter for the Au@TiO$_2$-5RS system, allowing in turn the subsequent prediction of NP size and f_{NP} for other filling fractions. This was employed for a more complex system such as the NP immersed in the titania layer of the bilayer system (Au10RS-TF/SC/glass).

4. CONCLUSIONS

Along this work, we set up the basis to model the plasmonic response of Au NP—without interactions—inside MTTF (TiO$_2$–F127). By experimental UV−visible spectrophotometry, we determine the LSPR of the system and the reduction steps that should be performed to consider isolated NP. We then conducted the modeling, analyzing each component—NP and MTTF—in detail. After this discussion, we were able to

model the NP@MTTF and to understand the appropriate way to describe it and compare it with experimental data.

Spectrometric Ellipsometry measurements provide accurately the dielectric function of the MTTF, that when used in the framework of Mie and Maxwell−Garnett theories leads to excellent agreement with UV−visible spectra of the nanocomposite NP@MTTF (see Figure 5 and Table 1). This technique also opens the possibility to acquire the full dielectric function of the nanocomposite systems, providing a precise result of the LSPR peak position, and thus enabling to study the response of the LSPR to the humidity present in the porosity. However, this technique supplies nanostructural information to determine the NP localization in a multilayer system and can be used to obtain the absorbance spectrum when a nontransparent substrate is used. We find out that this conversion gives exact results for dyes adsorbed in the MTTF, as detailed in the SI.

A valuable output of this modeling method is the excellent agreement between the proposed model and the actual experimental data. This permitted us to follow NP growth and assess NP size and filling fraction with a high degree of confidence. This has proven to be particularly interesting in understanding the role of synthesis variables in the reproducible production of NP@mesoporous oxide films, as well as proposing a plausible mechanism of formation of these nanocomposites.

Finally, and as a consequence of this work, it is worth to mention that this modeling strategy can be applied to other systems. In particular, we are investigating Ag@TiO$_2$ and Ag@SiO$_2$, where the modeling is more complex due to the reactivity of Ag NP that get usually oxidized in air conditions. These NP evolves to core−shell like structures Ag/Ag$_2$O NP[82] and constitute our current challenges to be modeled.

ASSOCIATED CONTENT

S Supporting Information

Detailed information regarding the film characterization is described including ellipsoporosimetry measurement, TEM and SAXS characterization of the MTTF and the calculation of pore filling fraction from EDS and from XRR measurements. FE−SEM images of the bilayer system Au10RS-TF/SC, calculated absorbance spectra using a Gaussian distribution function accounting for the polydispersity in particle size. Comparison between ellipsometry and UV−vis spectra in dye loaded MTTF. Additional TEM images of Au nanoparticles embedded in MTTF. This material is available free of charge via the Internet at http://pubs.acs.org.

AUTHOR INFORMATION

Corresponding Author
*Tel: (+54 11) 6772-7032; e-mail: gsoler@cnea.gov.ar.

Notes
The authors declare no competing financial interest.

ACKNOWLEDGMENTS

REFERENCES

(1) Chen, X.; Mao, S. S. Titanium Dioxide Nanomaterials: Synthesis, Properties, Modifications, And Applications. *Chem. Rev.* **2007**, *107*, 2891−2959.

(2) Diebold, U. The Surface Science Of Titanium Dioxide. *Surf. Sci. Rep.* **2003**, *48*, 53−229.

(3) Kamat, P. V. TiO$_2$ Nanostructures: Recent Physical Chemistry Advances. *J. Phys. Chem. C* **2012**, *116*, 11849−11851.

(4) Grätzel, M. Sol-Gel Processed TiO$_2$ Films for Photovoltaics Applications. *J. Sol-Gel Sci. Tech.* **2001**, *22* (1−2), 7−13.

(5) Linsebigler, A. L.; Lu, G.; Yates, J. T. Photocatalysis on TiO$_2$ Surfaces: Principles, Mechanisms, and Selected Results. *Chem. Rev.* **1995**, *95*, 735−758.

(6) Mayer, K. M.; Hafner, J. H. Localized Surface Plasmon Resonance Sensors. *Chem. Rev.* **2011**, *111*, 3828−3857.

(7) Domansky, K.; Liu, J.; Wang, L. Q.; Engelhard, M. H.; Baskaran, S. Chemical Sensors Based on Dielectric Response of Functionalized Mesoporous Silica Films. *J. Mater. Res.* **2001**, *16*, 2810−2816.

(8) Homola, J. Surface Plasmon Resonance Sensors for Detection of Chemical and Biological Species. *Chem. Rev.* **2008**, *108*, 462−493.

(9) Alivisatos, P. The Use Of Nanocrystals In Biological Detection. *Nat. Biotechnol.* **2004**, *22*, 47−52.

(10) Stewart, M. E.; Anderton, C. R.; Thompson, L. B.; Maria, J.; Gray, S. K.; Rogers, J. A.; Nuzzo, R. G. Nanostructured Plasmonic Sensors. *Chem. Rev.* **2008**, *108*, 494−521.

(11) Halas, N. J.; Lal, S.; Chang, W.-S.; Link, S.; Nordlander, P. Plasmons in Strongly Coupled Metallic Nanostructures. *Chem. Rev.* **2011**, *111*, 3913−3961.

(12) Ko, H.; Singamaneni, S.; Tsukruk, V. V. Nanostructured Surfaces and Assemblies as SERS Media. *Small* **2008**, *4*, 1576−1599.

(13) Lal, S.; Grady, N. K.; Kundu, J.; Levin, C. S.; De, J. B. L.; Halas, N. J. Tailoring plasmonic substrates for surface enhanced spectroscopies. *Chem. Soc. Rev.* **2008**, *37*, 898−911.

(14) Chumanov, G.; Sokolov, K.; Gregory, B. W.; Cotton, T. M. Nanostructured Surfaces and Assemblies as SERS Media. *J. Phys. Chem.* **2002**, *99*, 9466−9471.

(15) Aroca, R. F.; Alvarez-Puebla, R. A.; Pieczonka, N.; Sanchez-Cortez, S.; Garcia-Ramos, J. V. Surface-Enhanced Raman Scattering on Colloidal Nanostructures. *Adv. Colloid Interface Sci.* **2005**, *116*, 45−61.

(16) Mazurenka, M.; Hamilton, S. M.; Unwin, P. R.; Mackenzie, S. R. In-Situ Measurement of Colloidal Gold Adsorption on Functionalized Silica Surfaces. *J. Phys. Chem. C* **2008**, *112*, 6462−6468.

(17) Fuertes, M. C.; Marchena, M.; Marchi, M. C.; Wolosiuk, A.; Soler-Illia, G. J. A. A. Controlled Deposition of Silver Nanoparticles in Mesoporous Single- or Multilayer Thin Films: From Tuned Pore Filling to Selective Spatial Location of Nanometric Objects. *Small* **2009**, *5* (2), 272−280.

(18) Pérez, M. D.; Otal, E.; Bilmes, S. A.; Soler-Illia, G. J. A. A.; Crepaldi, E. L.; Grosso, D.; Sanchez, C. Growth of Gold Nanoparticle Arrays in TiO$_2$ Mesoporous Matrixes. *Langmuir* **2004**, *20*, 6879−6886.

(19) (a) Martínez, E. D.; Bellino, M. G.; Soler-Illia, G. J. A. A. Patterned Production of Silver-Mesoporous Titania Nanocomposite Thin Films Using Lithography-Assisted Metal Reduction. *ACS Appl. Mater. Interf.* **2009**, *1*, 746−749. (b) Martinez, E. D.; Granja, L.; Bellino, M. G.; Soler-Illia, G. J. A. A. Electrical Conductivity In Patterned Silver−Mesoporous Titania Nanocomposite Thin Films: Towards Robust 3D Nano-Electrodes. *Phys. Chem. Chem. Phys.* **2010**, *12*, 14445−14448.

(20) Angelomé, P. C.; Pastoriza-Santos, I.; Pérez-Juste, J.; Rodríguez-González, B.; Zelcer, A.; Soler-Illia, G. J. A. A.; Liz-Marzán, L. M. Growth And Branching Of Gold Nanoparticles Through Mesoporous Silica Thin Films. *Nanoscale* **2012**, *4*, 931−939.

(21) Angelomé, P. C.; Liz-Marzán, L. M. Monitoring Solvent Evaporation from Thin Films by Localized Surface Plasmon Resonance Shifts. *J. Phys. Chem. C* **2010**, *114*, 18379−18383.

(22) Subramanian, V.; Wolf, E. E.; Kamat, P. V. Catalysis with TiO_2/Gold Nanocomposites. Effect of Metal Particle Size on the Fermi Level Equilibration. *J. Am. Chem. Soc.* **2004**, *126* (15), 4943−4950.

(23) Lee, J.; Mubeen, S.; Ji, X.; Stucky, G. D.; Moskovits, M. Plasmoni Photoanodes for Solar Water Splitting with Visible Light. *Nano Lett.* **2012**, *12*, 5014−5019.

(24) Atwater, H. A.; Polman, A. Plasmonics for Improved Photovoltaic Devices. *Nature Mat.* **2010**, *9*, 205−213.

(25) Reineck, P.; Lee, G. P.; Brick, D.; Karg, M.; Mulvaney, P.; Bach, U. A Solid-State Plasmonic Solar Cell Via Metal Nanoparticle Self-Assembly. *Adv. Mater.* **2012**, *24* (35), 4750−4755.

(26) Li, X.; Chen, G.; Yang, L.; Jin, J.; Liu, J. Multifunctional Au-Coated TiO_2 Nanotube Arrays as Recyclable SERS Substrates for Multifold Organic Pollutants Detection. *Adv. Func. Mat.* **2010**, *20*, 2815−2824.

(27) Rebrov, E. V.; Berenguer-Murcia, A.; Johnson, B. F. G.; Schouten, J. C. Gold Supported on Mesoporous Titania Thin Films for Application in Microstructured Reactors in Low-Temperature Water-Gas Shift Reaction. *Catal. Today* **2008**, *138*, 210−215.

(28) Li, H.; Bian, Z.; Zhu, J.; Huo, Y.; Li, H.; Lu, Y. Mesoporous Au/TiO_2 Nanocomposites with Enhanced Photocatalytic Activity. *J. Am. Chem. Soc.* **2007**, *129*, 4538−4539.

(29) Creighton, J. A.; Eadont, D. G. Ultraviolet−Visible Absorption Spectra Of The Colloidal Metallic Elements. *J. Chem. Soc. Faraday. Trans.* **1991**, *87*, 3881−3891.

(30) Haiss, W.; Thanh, N. T. K.; Aveyard, J.; Fernig, D. G. Determination Of Size And Concentration Of Gold Nanoparticles From UV−Vis Spectra. *Anal. Chem.* **2007**, *79*, 4215−4221.

(31) Bhat, R. R.; Genzer, J. Using Spectroscopic Ellipsometry For Quick Prediction Of Number Density Of Nanoparticles Bound To Non-Transparent Solid Surfaces. *Surf. Sci.* **2005**, *596*, 187−196.

(32) Losurdo, M.; Bergmair, M.; Bruno, G.; Cattelan, D.; Cobet, C.; Martino, A.; Fleischer, K.; Dohcevic-Mitrovic, Z.; Esser, N.; Galliet, M.; et al. Spectroscopic Ellipsometry and Polarimetry for Materials and Systems Analysis at the Nanometer Scale: State-of-the-Art, Potential and Perspectives. *J. Nanoparticle Res.* **2009**, *11* (7), 1521−1554.

(33) Kürbitz, S.; Postendorfer, J.; Berg, K. J.; Berg, G. Determination Of Size And Concentration Of Copper Nanoparticles Dispersed In Glasses Using Spectroscopic Ellipsometry. *Appl. Phys. B: Laser Opt.* **2001**, *73*, 333−337.

(34) Oates, T. W. H.; Wormeester, H.; Arwin, H. Characterization of Plasmonic Effects in Thin Films and Metamaterials Using Spectroscopic Ellipsometry. *Prog. Surg. Sci* **2011**, *86*, 328−376.

(35) Zhang, Y.; Yuwono, A. H.; Li, J.; Wang, J. Highly Dispersed Gold Nanoparticles Assembled in Mesoporous Titania Flms of Cubic Configuration. *Microporous Mesoporous Mater.* **2008**, *110*, 242−249.

(36) Mie, G.. Contributions to The Optics of Turbid Media, Particularly of Colloidal Metal Solutions. *Ann. Physik* **1908**, *25*, 377−445.

(37) Garnett, J. C. M. Colours in Metal Glasses and in Metallic Films. *Philos. Trans. R. Soc. Lond.* **1904**, *203*, 385−420.

(38) Sepúlveda, B.; Angelomé, P. C.; Lechuga, L. M.; Liz-Marzán, L. M. LSPR-based Nanobiosensors. *Nano Today* **2009**, *4*, 244−251.

(39) Gehan, H.; Mangeney, C.; Aubard, J.; Lévi, G.; Hohenau, A.; Krenn, J. R.; Lacaze, E.; Félidj, N. Design and Optical Properties of Active Polymer-Coated Plasmonic Nanostructures. *J. Phys. Chem. Lett.* **2011**, *2*, 926−931.

(40) Soler-Illia, G. J. A. A.; Sanchez, C.; Lebeau, B.; Patarin, J. Chemical Strategies To Design Textured Materials: from Microporous and Mesoporous Oxides to Nanonetworks and Hierarchical Structures. *Chem. Rev.* **2002**, *102*, 4093−4138.

(41) Crepaldi, E. L.; Soler-Illia, G. J. A. A.; Grosso, D.; Cagnol, F.; Ribot, F.; Sanchez, C. Controlled Formation of Highly Organized Mesoporous Titania Thin Films: From Mesostructured Hybrids to Mesoporous Nanoanatase TiO_2. *J. Am. Chem. Soc.* **2003**, *125*, 9770−9786.

(42) Martínez Ricci, M. L.; Fuertes, M. C.; Violi, I. L.; Grosso, D.; Boissiere, C.; Sanchez, C.; Soler-Illia, G. J. A. A.Ordered Mesoporous Thin Films Through Fast Post-Synthetic Treatment. Work in progress, provided as Reviewer-Only information.

(43) Boissiere, C.; Grosso, D.; Lepoutre, S.; Nicole, L.; Bruneau, A. B.; Sanchez, C. Porosity and Mechanical Properties of Mesoporous Thin Films Assessed by Environmental Ellipsometric Porosimetry. *Langmuir* **2005**, *21*, 12362−12371.

(44) Angelomé, P. C.; Fuertes, M. C.; Soler-Illia, G. J. A. A. Multifunctional, Multilayer, Multiscale: Integrative Synthesis of Complex Macroporous and Mesoporous Thin Films with Spatial Separation of Porosity and Function. *Adv. Mater.* **2006**, *18*, 2397−2402.

(45) Thompkins, H. G.; McGahan, W. A. *Spectroscopic Ellipsometry and Reflectometry*; Wiley: New York, 1999.

(46) Bass, M.; Mahajan, V. N.; Van Stryland, E., Handbook of Optics: Design, Fabrication, and Testing; Sources and Detectors; Radiometry and Photometry. McGraw-Hill Professional: Columbus, OH, 2009; Vol. 4.

(47) Oates, T. W. H. Real Time Spectroscopic Ellipsometry Of Nanoparticle Growth. *Appl. Phys. Lett.* **2006**, *88*, 2006−2008.

(48) Bass, J.; Grosso, D.; Boissiere, C.; Sanchez, C. Pyrolysis, Crystallization, and Sintering of Mesostructured Titania Thin Films Assessed by In Situ Thermal Ellipsometry. *J. Am. Chem. Soc.* **2008**, *3*, 787−792.

(49) Angelome, P. C.; Andrini, L.; Calvo, M. E.; Requejo, F. G.; Bilmes, S. A.; Soler-Illia, G. J. A. A. Mesoporous Anatase TiO_2 Films: Use of Ti K XANES for the Quantification of the Nanocrystalline Character and Substrate Effects in the Photocatalysis Behavior. *J. Phys. Chem. C* **2007**, *111*, 10886−10893.

(50) Violi, I. L.; Perez, M. D.; Fuertes, M. C.; Soler-Illia, G. J. A. A. Highly Ordered, Accessible and Nanocrystalline Mesoporous TiO_2 Thin Films on Transparent Conductive Substrates. *ACS Appl. Mater. Interfaces* **2012**, *4*, 4320−4330.

(51) Soler-Illia, G. J. A. A.; Angelomé, P. C.; Fuertes, M. C.; Grosso, D.; Boissiere, C. Critical Aspects In The Production Of Periodically Ordered Mesoporous Titania Thin Films. *Nanoscale* **2012**, *4*, 2549−2566.

(52) Kreibig, U.; Vollmer, M. *Optical Properties of Metal Clusters*; Springer: New York, 1995.

(53) Lin, Q.; Sun, Z. Study on Optical Properties of Aggregated Ultra-Small Metal Nanoparticles. *Optik* **2011**, *122*, 1031−1036.

(54) Jain, P. K.; Huang, W.; El-Sayed, M. A. On the Universal Scaling Behavior of the Distance Decay of Plasmon Coupling in Metal Nanoparticle Pairs: A Plasmon Ruler Equation. *NanoLetters* **2007**, *7*, 2080−2088.

(55) Liu, Z.; Wang, H.; Li, H.; Wang, X. Red Shift of Plasmon Resonance Frequency Due to the Interacting Ag Nanoparticles Embedded in Single Crystal SiO_2 by Implantation. *Appl. Phys. Lett.* **1998**, *72*, 1823−1825.

(56) Ung, T.; Liz-Marzán, L. M.; Mulvaney, P. Optical Properties of Thin Films of Au@SiO_2 Particles. *J. Phys. Chem. B* **2001**, *105*, 3441−3452.

(57) Dalacu, D.; Martinu, L. Spectroellipsometric Characterization of Plasma-Deposited Au/SiO_2 Nanocomposite Films. *J. Appl. Phys.* **2000**, *87*, 228−235.

(58) Hutchinson, N. J.; Coquil, T.; Navid, A.; Pilon, L. Effective Optical Properties of Highly Ordered Mesoporous Thin Films. *Thin Solid Films* **2010**, *518*, 2141−2146.

(59) Sihvola, A. *Electromagnetic Mixing Formulas and Applications, IEE Electromagnetic Waves Series*; The Institution of Electrical Engineers: London, 1999; Vol. 47.

(60) Mulvaney, P. Surface Plasmon Spectroscopy of Nanosized Metal Particles. *Langmuir* **1996**, *12*, 788−800.

(61) Kelly, K. L.; Coronado, E.; Zhao, L. L.; Schatz, G. C. The Optical Properties of Metal Nanoparticles: The Influence of Size, Shape, and Dielectric Environment. *J. Phys. Chem. B* **2003**, *107*, 668−677.

(62) Jensen, T. R.; Duval, M. L.; Kelly, K. L.; Lazarides, A. A.; Schatz, G. C.; Van Duyne, R. P. Nanosphere Lithography: Effect of the External Dielectric Medium on the Surface Plasmon Resonance

Spectrum of a Periodic Array of Silver Nanoparticles. *J. Phys. Chem. B* **1999**, *103*, 9846−9853.

(63) Jain, P. K.; El-Sayed, M. A. Plasmonic Coupling In Noble Metal Nanostructures. *Chem. Phys. Lett.* **2010**, *487*, 153−164.

(64) Lee, K-S; El-Sayed, M. A. Gold and Silver Nanoparticles In Sensing and Imaging: Sensitivity of Plasmon Response to Size, Shape, and Metal Composition. *J. Phys. Chem. B* **2006**, *110*, 19220−19225.

(65) Noguez, C. J. Surface Plasmons on Metal Nanoparticles: The Influence of Shape and Physical Environment. *J. Phys. Chem. C.* **2007**, *111*, 3806−3819.

(66) Link, S.; El-Sayed, M. A. Spectral Properties and Relaxation Dynamics of Surface Plasmon Electronic Oscillations in Gold and Silver Nanodots and Nanorods. *J. Phys. Chem. B* **1999**, *103*, 8410−8426.

(67) Prodan, E.; Nordlander, P. Plasmon Hybridization in Spherical Nanoparticles. *J. Chem. Phys.* **2004**, *120*, 5444−5454.

(68) Wang, J.; Lau, W.; M. Li, Q. Effects Of Particle Size and Spacing on the Optical Properties of Gold Nanocrystals in Alumina. *J. Appl. Phys.* **2005**, *97*, 114303−114308.

(69) Lermé, J. Size Evolution of the Surface Plasmon Resonance Damping in Silver Nanoparticles: Confinement and Dielectric Effects. *J. Phys. Chem. C.* **2011**, *115*, 14098−14110.

(70) Yang, P.; Portalès, H.; Pileni, M.-P. Dependence of the Localized Surface Plasmon Resonance of Noble Metal Quasispherical Nanoparticles on Their Crystallinity-Related Morphologies. *J. Chem. Phys.* **2011**, *134*, 24507.

(71) Hövel, H.; Fritz, S.; Hilger, A.; Kreibig, U.; Vollmer, M. With of Cluster Plasmon Resonances: Bulk Dielectric Functions and Chemical Interface Damping. *J. Am. Phys. Soc.* **1993**, *48*, 18178−18187.

(72) Garcia, M. A. Surface Plasmons in Metallic Nanoparticles: Fundamentals and Applications. *J. Phys. D: Appl. Phys.* **2011**, *44*, 283001.

(73) Hilger, A.; Tenfelde, M.; Kreibig, U. Silver Nanoparticles Deposited On Dielectric Surfaces. *Appl. Phys. B: Laser Opt.* **2001**, *73*, 361−372.

(74) Palik. E. D. *Handbook of Optical Constant of Solids*; Academic Press: New York, 1998.

(75) Johnson, P. B.; Christy, R. W. Optical Constants of the Noble Metals. *Phys. Rev. B.* **1972**, *6*, 4370−4379.

(76) Maier,S. A. *Plasmonics: Fundamentals and Applications*; Springer: New York, 2007.

(77) Bahadur, N.; Jain, K.; Pasricha, R.; Govind; Chandet, S. Selective Gas Sensing Response From Different Loading of Ag in Sol−Gel Mesoporous Titania Powders. *Sens. Actuators, B* **2011**, *159*, 112−120.

(78) Calvo, A.; Fuertes, M. C.; Yameen, B.; Williams, F. J.; Azzaroni, O.; Soler-Illia, G. J. A. A. Nanochemistry in Confined Environments: Polyelectrolyte Brush-Assisted Synthesis of Gold Nanoparticles Inside Ordered Mesoporous Thin Films. *Langmuir* **2010**, *26*, 5559−5567.

(79) It is well-known that these mesopores are of an ellipsoidal shape, due to uniaxial contraction. Typical uniaxial shrinkages of the mesopore structure are in the order of 40−50%, the pore height being in the order of 5−6 nm.[35] This supports the hypothesis (b), i.e., that filled pores contain asymmetric particles. Interestingly, the spherical model explains very accurately the optical properties when NP are below 6 nm diameter.

(80) Polder, D.; Van Santen, J. H. The Effective Permeability of Mixtures of Solids. *Physica* **1946**, *12*, 257−271.

(81) García, A.; Llopis, J.; Paje, E. A Simple Model for Evaluating the Optical Absorption Spectrum From Small Au-Colloids in Sol−Gel films. *Chem. Phys. Lett.* **1999**, *315*, 313−320.

(82) Schinca, D. C.; Scaffardi, L. B.; Videla, F. A.; Torchia, G. A.; Moreno, P.; Roso, L. Silver−Silver Oxide Core−Shell Nanoparticles By Femtosecond Laser Ablation: Core and Shell Sizing by Extinction Spectroscopy. *J. Phys. D: Appl. Phys.* **2009**, *42*, 215102.